Improved fibre placement in filament-based 3D printing of continuous carbon fibre reinforced thermoplastic composites

Improved fibre placement in filament-based 3D printing of continuous carbon fibre reinforced thermoplastic composites

Ka Zhang, Haoqi Zhang, Jiang Wu, Jiayun Chen, Dongmin Yang*

Institute for Materials and Processes, School of Engineering, University of Edinburgh, EH9 3FB, UK

Abstract

This study investigates the mechanism of fibre deposition in conventional 3D printing and presents an aligned fibre deposition (AFD) method to improve the fibre placement. The deposition mechanism reveals that the cracking of the filament in the transition zone and the torsional deformation during the steering path are the main cause of the defects in the conventional printing process. The AFD method is shown to reduce and mitigate the fibre waviness and twisting, hence producing smooth filament deformation, introducing less air voids and fibre breakage during printing. It is found that the AFD method improves the fibre alignment angle from $\pm 25°$ to $\pm 12°$ and reduces the void content to 0.27% during straight-line deposition. During curved-line printing at a large radius of curvature, tow shearing instead of fibre folding is produced by AFD method, resulting in smooth edges with less fibre breakage.

Keywords: 3D printing; Aligned fibre deposition; Fibre misalignment; Tow shearing.

* Corresponding author. Email: Dongmin.Yang@ed.ac.uk

1. Introduction

3D printing of continuous carbon fibre-reinforced thermoplastic polymer composites (cCFRP) has been gaining rapid momentum across a number of industrial sectors including aerospace, automotive and sporting goods [1]. Commercialised bench-top material extrusion based printers [2, 3] are available on market for printing branded cCFRP filaments. In-house printers have also been developed using in-nozzle impregnation methods to print custom-made composite filament of continuous fibres and thermoplastic matrix [4, 5]. Besides, multi-axis gantry systems [6] and robotic arms [7] have been used to assist the printing of large composite structures with more complex shapes by increasing the degree of freedom for the printer head and thus becoming more similar with the automated tape/fibre placement (ATP/AFP) [8] which have existed for decades before 3D printing emerged in composites industry. Whilst ATP/AFP has been mainly adopted in aerospace industry to place large fibre tapes (above 6K fibre bundle), 3D printing of cCFRP using filament with small fibre bundle (*e.g.*, 1K or 3K, see Fig. 1a) has the potential to manufacture high precision composites with complex shapes at a lower cost [9].

However, current 3D printing methods for cCFRP still face a few critical challenges before reaching their full potential, such as fibre misalignment [10], fibre breakage [11, 12], fibre folding [13] as well as high void content during the deposition process. Printing defects have been observed in our previous experimental work [10]: (i) fibre waviness/misalignment occurs even when printing a straight path (see Fig. 1b); (ii) fibre twisting/folding occurs at curved sections (see X-ray computed microtomography image in Fig. 1c); and (iii) printed stripe size (width and thickness) is inconsistent, resulting in poor geometric accuracy of the printed part.

Different to the ATP/AFP process in which the carbon fibre tows are normally prepared as tapes and pressed using a soft compact roller, the cylindrical filament used in most 3D printing processes is pressed into a thin stripe, which involves a more significant change of shape and thus more complicated stress re-distribution. Fibre misalignment would occur because of the severe deformation of fibre bundle [14]. Fibre folding, on the other hand, which is thought to be caused by the tensile force of filament during printing [15], would trigger fibre breakage and reduce the precision of the

printed radius [13]. This is different to the fibre wrinkling or fibre buckling on the inner side of the curved tape that occurs in the tape placement process of ATP/AFP. Small radii of curvature of 4 mm and 5 mm have been achieved using the 1K and 8K fibre filaments [13], respectively, making 3D printing distinctive to AFP that normally produces a large radius of over 500 mm for 24K tows [16]. Hence, it is worth investigating the formation of defects and improving the deposition process in 3D printing of cCFRP.

Fig. 1 X-ray computed microtomography (μCT) of composite filament: (a) 3D view of the raw filament with matrix hidden, top view of (b) the printed filament in a straight path, and (c) the printed filament at a curved section with a turning angle of 90° [10].

Hirohide *et al*. [15] have observed the deposition process through a mirror, but the printing mechanism of such composite filament is not fully understood due to the low resolution of observation. So far there is still a knowledge gap in holistically establishing a more appropriate deposition method, such as nozzles as well as printing systems, to improve the fibre deposition, although some works have tried to explore new printing processes [17].

In this paper, a most popular fibre deposition process of filament-based 3D printing is theoretically investigated and an aligned fibre printing/deposition system is proposed and developed to mitigate the aforementioned printing defects. Both straight and curved paths are printed, characterised, and then compared with those from the traditional printing method. Furthermore, evolution of the fibre bundle of these two printing methods is experimentally observed and numerically simulated to uncover the mechanism of the deposition process. The paper is organised as follows. In section 2, a theoretical analysis is carried out on the current fibre deposition methods and a new disposition method is proposed. Section 3 introduces the methodologies to comprehensively compare these two deposition methods. Section 4 presents the characterisation results of printed filaments. Section 5 interprets the deposition mechanisms. Finally, main conclusions are drawn in Section 6.

2. Fibre deposition methods

2.1 Current fibre deposition methods

The most popular fibre deposition methods for 3D printing of continuous fibres currently use a cylindrical nozzle which directly evolves from those used for neat thermoplastic [18]. For example, Mark Two® uses a cylindrical brass nozzle ('M-nozzle') with an enlarged conical outlet and a ring-like flat tip for its carbon fibre filament, as shown in Fig. 2a. The inner edge of the nozzle tip is rounded to facilitate the feeding and bending of the vertical filament to the flat compression plane. Continuous carbon fibre filaments are normally 1K or 3K fibre bundles [13, 19]. During the deposition, the filament is vertically fed into the nozzle (*i.e.*, vertical fibre deposition), and then bent and compressed by the nozzle tip to bond with the printer bed or the substrate layers. A deformed elbow is formed where the cylindrical filament is bent and compressed. This area, which is called the transition zone (in Fig. 2a), is thus the critical region of interest for investigating the microstructure of the printed fibre bundle (fibre misalignment/waviness and fibre folding).

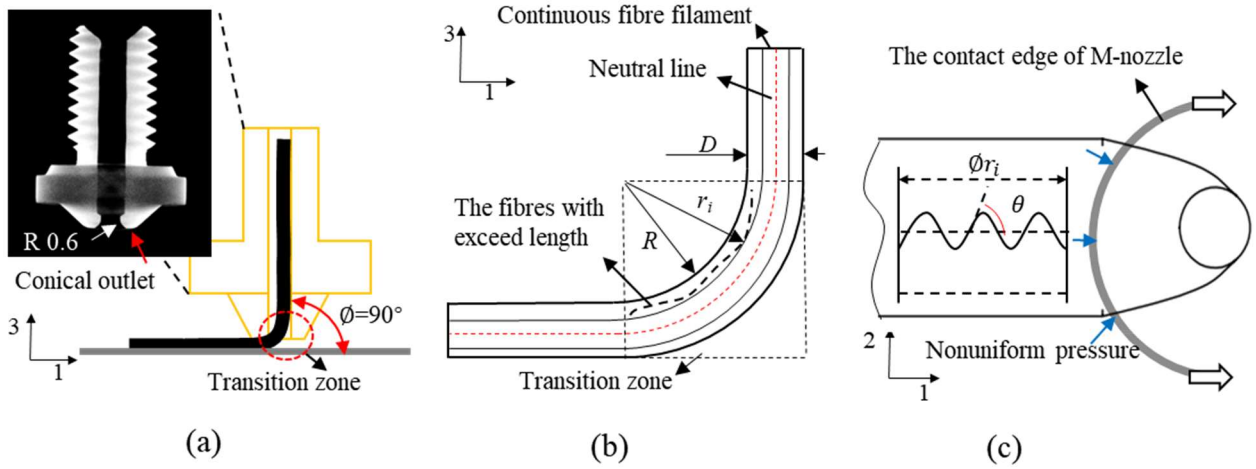

Fig. 2 (a) Schematic deposition process using M-nozzle, (b) bending deformation of the filament and (c) the contact of filament and nozzle tip

The large bending deformation caused by the vertical feeding passage would lead to longitudinal compression and tension at the elbow of the filament and cause unequal fibre lengths. Fibre waviness would then occur due to the compression of the fibres with excess lengths, which also makes the interaction points between fibres much complicated before they are compressed by the nozzle tip. Studies [14, 20, 21] have shown that fibre misalignment and waviness are related to the deformation of fibre networks and their contact points during compression. For the vertical deposition methods,

the fibre bundle is not aligned in the first place before compression because of the bending deformation. The non-aligned fibre contact points would aggravate the fibre waviness and misalignment.

Fibres at the inner periphery of the bending filament are under compression and causing fibre waviness, while fibres at the outer periphery may be pulled to move due to the tension (see Fig. 2b). Considering the central line of the filament as a neutral line where the fibres rarely move, the fibre length at the radius of r_i is equal to the length of neutral line, and can be calculated [22] as:

$$L_{\text{fiber}} = \int_0^{\emptyset r_i} \sqrt{1 + \left(\frac{\mathrm{d}_y}{\mathrm{d}_x}\right)^2}\, \mathrm{d}_x = \frac{1}{2}\emptyset(D + 2R) \tag{1}$$

Where $\frac{\mathrm{d}_y}{\mathrm{d}_x}$ is the differential of a $y = A\sin(\omega x + \varphi)$ type waved fibre; D and R are the diameter and inner radius of the filament elbow, respectively. The bending angle is $\emptyset = \frac{\pi}{2}$ for the vertical deposition method.

Suppose there are n cycles within the integral length $\emptyset r_i$, hence $\omega = \frac{2n\pi}{\emptyset r_i}$. The length of waved fibres at radius r_i can be derived as:

$$L_{\text{fibre}} = \frac{2\emptyset r_i}{\pi}\sqrt{1 + \alpha^2} \cdot E\left(\frac{\alpha^2}{1+\alpha^2}\right) \tag{2}$$

Where $E(m)$ is the elliptic integral of the second kind; and $\alpha = A\omega$.

The maximum excess length of waved fibre exists when the radius equals to R, and it can be expressed as:

$$L_{\text{max\_excess\_length}} = L_{\text{fiber}} - \emptyset R = \frac{1}{2}\emptyset D \tag{3}$$

The maximum excess length of fibre can be derived by substituting Eq. (2) into (3):

$$\frac{1}{2}\emptyset D = \emptyset\frac{2R}{\pi}\left[\sqrt{1 + \alpha^2} \cdot E\left(\frac{\alpha^2}{1+\alpha^2}\right) - \frac{\pi}{2}\right] \tag{4}$$

Eq. (4) can be rearranged as:

$$\frac{D\pi}{4R} = \sqrt{1 + \alpha^2} \cdot E\left(\frac{\alpha^2}{1+\alpha^2}\right) - \frac{\pi}{2} \tag{5}$$

While the maximum misalignment angle caused by the excess fibres can be calculated by the derivative of the sine curve:

$$\alpha = \tan(\theta_{\max}) \tag{6}$$

Eq. (5) can be written as the following, when substituting Eq. (6) into it:

$$\frac{D\pi}{4R} = \sqrt{1+\tan(\theta_{\max})^2} \cdot E\left(\frac{\tan(\theta_{\max})^2}{1+\tan(\theta_{\max})^2}\right) - \frac{\pi}{2} \quad (7)$$

Obviously, the maximum alignment angle is related to the bending radius R and the filament diameter D. Considering the right-hand side of Eq. (7) as a function $f(\theta_{max})$, which can be proved as a monotonic increasing function by plotting the curve in MATLAB. This shows that the fibre alignment can be improved by increase R or reducing D. However, for the current printing methods, increasing R means the use of a larger nozzle size. An alternative way is to feed the filament through a passage at an inclined angle which could increase the bending radius without increasing the nozzle size. A smaller diameter of filament would also help the fibre deposition. The thin tapes for the traditional fibre placement can cause less fibre misalignment than the cylindrical filament, but it is more challenging to steer tapes than filament because of the fibre wrinkling issue [23]. Furthermore, it is practically easier to manufacture filaments rather than thin tapes using 1K or 3K fibre tows.

The non-rotational movement of the deposition methods could be the main reason causing fibre twisting and fibre folding because the fibre bundle is not aligned in its placement direction. The inversion of the inner and outer circumferences of the fibre bundle would occur twice when a circle is printed [13]. The fibre filament should twist along with the printing path to avoid the fibre folding and twisting.

Furthermore, the conical outlet of the M-nozzles would have an edge effect on the printed stripe. The ring-like nozzle tip squeezes the filament as it moves forward. The deformed tow would be pressed by the side of the edges, as shown in Fig. 2c, which would cause a non-uniform pressure distribution along the width direction. As such, fibre waviness and waved edges could be further exacerbated.

2.2 Aligned fibre deposition (AFD) method

Based on the above theoretical analysis, a rotational nozzle ('R-nozzle') with an inclined passage (45°) and a rectangle outlet is designed (see Fig. 3a). The bending radius is increased to 2.5 mm comparing to the 0.6 mm of M-nozzle, thanks to the inclined passage. The rectangular outlet ensures that the filament can be pressed evenly by the rounded rear edge of the nozzle tip to mitigate edge effects. The width of the rectangle is 0.8 mm, which is slightly narrow than the placed stripe (around 1.2 mm, referring to a previous study [10]) to enable a smooth extension of the filament in its width

and limit the wobble of the filament to achieve higher deposition accuracy. The other edge of the rectangle is 0.6 mm, which is reasonably larger than the diameter of the filament (*i.e.*, 0.375 mm) to ensure a pass-through at the start of the printing.

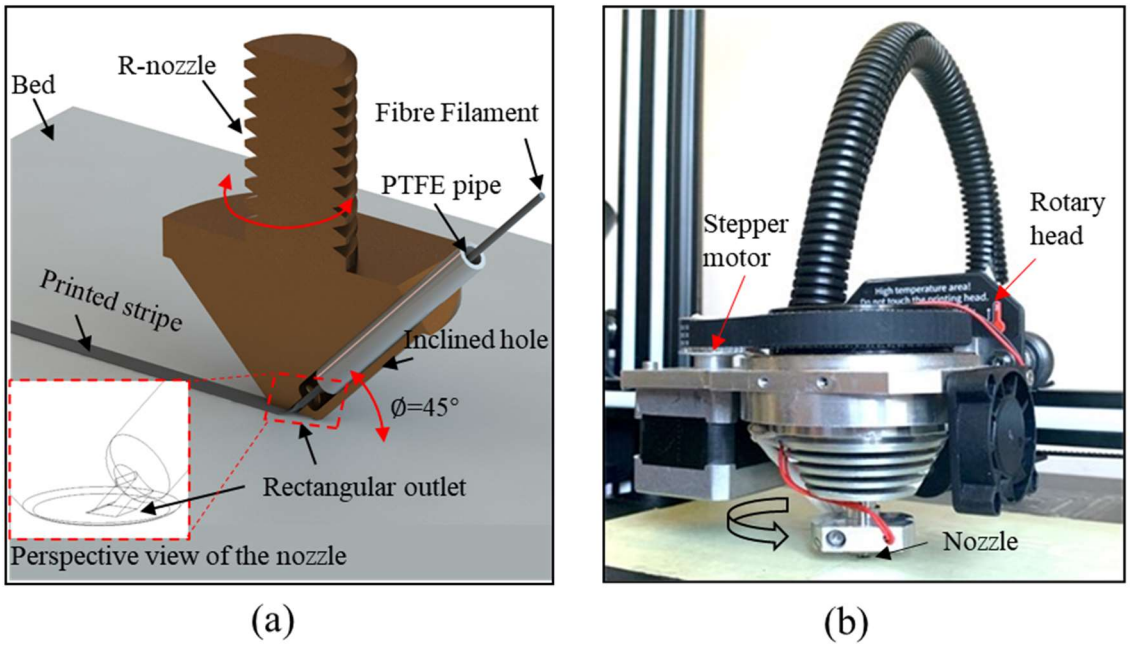

Fig. 3 (a) Schematic of the new-designed nozzle and (b) the rotational printing system.

During the printing process, the printing direction of the new nozzle needs to be aligned with the fibre placement direction because of its rectangular outlet. Therefore, a rotational printer head is designed and mounted on a modified printer (Geeetech A30m), as shown in Fig. 3b. More specifically, the stepper motor for the extruder of the 3D printer is used to drive the rotational head. Therefore, the rotational head can be easily controlled by simply replacing the coordinate values for the extruder in the G-code. These values can be calculated from the angle the head is rotated from its home position. In this study, the home position of the rotational head is defined as the position where the placement direction of the nozzle is aligned with the *x*-axis. During printing, the placement direction of the nozzle is aligned with the tangent vector of a path. Hence, the angle between the tangent vector at any points and *x*-axis is the angle needs to be calculated. It is worth mentioning that the machine configurations, such as gear diameters, extruder reduction ratios, also need to be considered when calculating the coordinate values. A customised Python program is developed to calculate the coordinates and modify the G-code. This printing method is named aligned fibre deposition (AFD). The header is guided to synchronously rotate with the movement in *x* and *y* directions to achieve a

smooth curved line. The working range of rotation is set as ± 360° and its runout tolerance of rotational movement is controlled below ± 0.1 mm.

3. Methodology

3.1 Printing paths

In this study, continuous carbon fibre filament is printed out along both straight and curved paths, to illustrate the performance of AFD method and compare with the conventional deposition method. Based on the parameters from previous studies [10, 13], a series of radii of curvature including 10.0 mm, 5.0 mm, 2.5 mm and 1.2 mm, are chosen to deposit curved paths. Before the curved section, a straight path longer than 100 mm is printed to ensure a stable deposition at the start, as shown in Fig. 4. The printed straight and curved stripes are characterised by investigating fibre alignment, tow morphology and fibre breakage, which is shown in section 4. The radius of 1.2 mm is set as the smallest curvature radius to explore the limitations of both two nozzles, as direct turning with large angles (no radius of curvature) should be avoided during printing due to the severe fibre folding and width change [10].

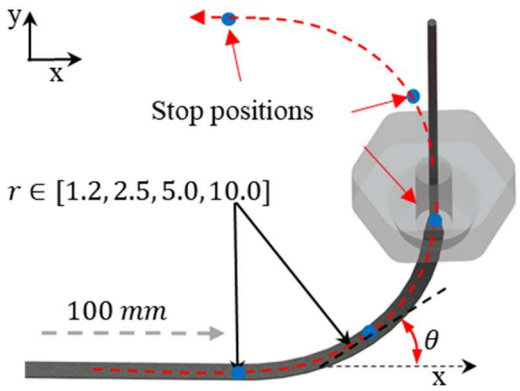

Fig. 4 Schematic diagram of a curved line in the printing experiment.

Besides, the transition zone of filament mentioned in last section is observed to fully understand the deposition process. Specifically, the printing process is deliberately paused at a series of positions and the deformed elbows of filament are then taken out and observed in scanning electron microscope (SEM). The fibre alignment and voids can be seen more clearly thanks to the high resolution of SEM. The obtained images will help reveal the evolution of aligned fibres for both printing methods. The samples are taken at the curvature radius of 2.5 mm for this observation because a larger deformation of filament can be seen at this radius compared to other radii. Five representative angular positions

($\theta = 0°, 45°, 90°, 135°$ and 180°) are chosen as the stop positions, and the nozzle lifts 5 mm quickly (600 mm/min) at each position to produce the deformed elbows. The printer is left to naturally cool down and then the printed stripe is cut off and taken out for examination. The results will be presented and discussed in Section 5.

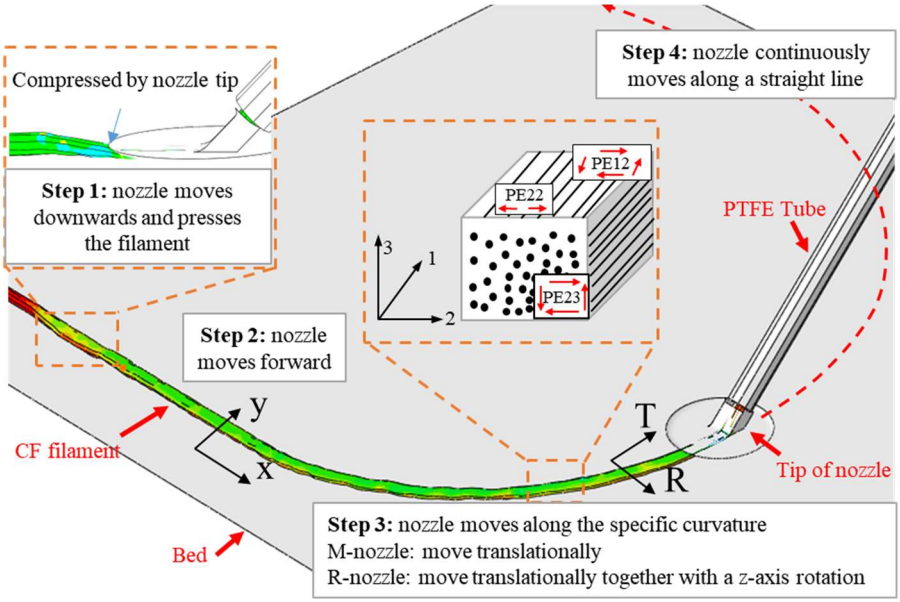

Fig. 5 The assembled FE model; Step 1: the cross-section of filament changes when the nozzle moves downwards and Steps 2-4: the printing process at a specific radius of curvature.

3.2 Filament material and printing parameters

Continuous carbon fibre reinforced thermoplastic filament (1K) from Markforged® is used for all experiments herein. It has been found the material is likely T300/polyamide 6 (PA6) [24]. The filament diameter is around 0.375 mm, and the fibre content is about 34% [25, 26]. The printing temperature is set to 235 ℃ with a printing speed of 300 mm/min. The filament is passively dragged into the printer head and its other end is intentionally left free to minimize the effect of the printer head on filament twisting because an active feeding mechanism would constrain the rotation of the filament and would cause fibre twisting [27]. The rotation is inactivated while using the M-nozzle for comparative trials, to replicate the printing process of the conventional printing methods (*i.e.*, no rotation).

3.3 Observation setup

Scanning electron microscope (SEM, JSM IT-200) and μCT (Nikon XT-H225) are used to observe the printed stripes. Those cases with a large radius of 10.0 mm are observed by SEM due to the projection limit of the μCT scanner. SEM photos of different sections are stitched together to clearly

show the curved stripes, allowing the analysis of fibre distribution, fibre breakage, and tow morphology. Other stripes are scanned by μCT for 3D viewing. A voltage of 60 kV and a power of 7 W is set to the μCT scanner to achieve the possibly best image quality with a resolution of 3192 x 2296 (voxel size of 3.058 μm). Each scan takes about 9 hours with 2D images projected at an increment of 3°. The images are produced and reconstructed into a 3D image using Avizo software. The individual fibres are traced to obtain the statistic of fibre misalignment and the air void fraction of the printed stripes are calculated by summing the volume of bubbles inside the stripes.

3.4 Finite element Modelling

The final geometry of fibre network after printing is hard to predict because of the unknown fibre contact point [20]. A finite element (FE) model is developed in ABAQUS to assist the performance comparison and the mechanism interpretation of these two printing methods. The compression of fibre bundle is known as a non-linear process [14, 28]. The strain distributions in the FE model will interpret the deformation of fibre bundle and the degree of fibre misalignment.

In real printing experiments, the original filament with a cylindrical shape is heated up in the heating block and the plastic matrix of the filament is softened. The printer nozzle exerts a contact pressure on the heated filament, changing the shape of the filament from cylindrical to roughly rectangular. As shown in Fig.5, this process is reasonably simplified in the FE model by using a cylindrical shape filament passing through a guide tube inserted in the nozzle. Only the tip of the nozzle, which is in contact with the filament, is simulated in the model for the purpose of reducing the computational cost. The simulation of the printing process with a specific curvature consists of 4 steps: (1) the nozzle moves downwards for 0.275 mm and presses the filament onto the printer bed, reaching an off distance of 0.1 mm; (2) the nozzle moves straight for a distance of 10 mm along the longitudinal direction of the deposited filament on the bed; (3) the nozzle moves translationally with a curvature radius of 2.5 or 10.0 mm; and (4) the nozzle moves forwards for 10 mm. More specifically, M-nozzle and R-nozzle move differently in Step 3 according to the real printing experiment, as shown in Fig.5. A small curvature radius of 2.5 mm and a large curvature radius of 10 mm are selected for the FE model, as they are more representative of the experimental observations.

The diameter of the cylindrical shape filament is 0.375 mm, and a total number of 160 C3D8R solid elements per millimetre are generated. The continuous carbon fibre filament is modelled as transversely isotropic with detailed material properties adopted from our previous work [10] and listed in Table 1. Low yielding stress (Y=10 MPa in simple tension) is defined for the initiation of the plastic strain so that the deformation of the heated composite filament (with melted PA6 matrix) during the printing process can be recorded as much as possible by the accumulated values of plastic strain. As measured from our experiments, there is no apparent volumetric change after the deposition, von Mises shear strain-energy yielding criterion with an associated plastic flow was adopted to account for the plastic deformation of the isotropic cross-section,

$$J_2 = \frac{1}{6}\{(\sigma_1 - \sigma_2)^2 + (\sigma_2 - \sigma_3)^2 + (\sigma_3 - \sigma_1)^2\} = \frac{Y^2}{3} \quad (8)$$

in which σ_1, σ_2 and σ_3 are the principal stresses.

All the plastic properties in the fibre direction are scaled by 60 times (*i.e.*, R_{11} = 60 in Table 1), considering the high modulus in the fibre direction even when the PA6 in the composite filament is melted. It should be noted that these plastic properties are reasonably assumed rather than obtained in the mechanical tests due to the difficulties of experimental measurement of such small filament at elevated temperatures. Thus, this model is built to compare these two different printing methods and further understand the deposition process[10].

Table 1. Elastic and plastic properties of the melted composite filament

E_1	E_2 & E_3	v_{12} & v_{13}	v_{23}	G_{12} & G_{13} & G_{23}	Initiation of plastic strain	Plastic strain = 1	R_{11}	R_{22} & R_{33} & R_{12} & R_{13} & R_{23}
31GPa	46MPa	0.2	0.39	5 GPa	Yield stress = 10 MPa	Yield stress = 100 MPa	60	1

4. Deposition performance

Straight and curved sections are printed according to the above setup. Only the middle parts of the printed filament are picked for scans and observations due to the projection area of the SEM and μCT equipment. The samples are marked as the M-nozzle case and the R-nozzle case respectively to distinguish the two different print methods.

4.1 Straight line

The µCT scanned straight stripes are shown in Fig. 6. For the M-nozzle case (see Fig. 6a), fibre misalignment, in particular in-plane waviness, is observed. Practically, the bottom fibres that are bonded with the bed have more dramatic waviness than the top, which may indicate higher stress concentrations on the bottom of the tape during printing. In contrast, significantly better fibre alignment is produced by R-nozzle (see Fig. 6b) compared to the M-nozzle, even though slight fibre misalignment still can be seen in the middle of the fibre bundle. The aligned fibre also leads to straight and consistent edges, making the printed filament a straight tape with a consistent dimension of width and thickness.

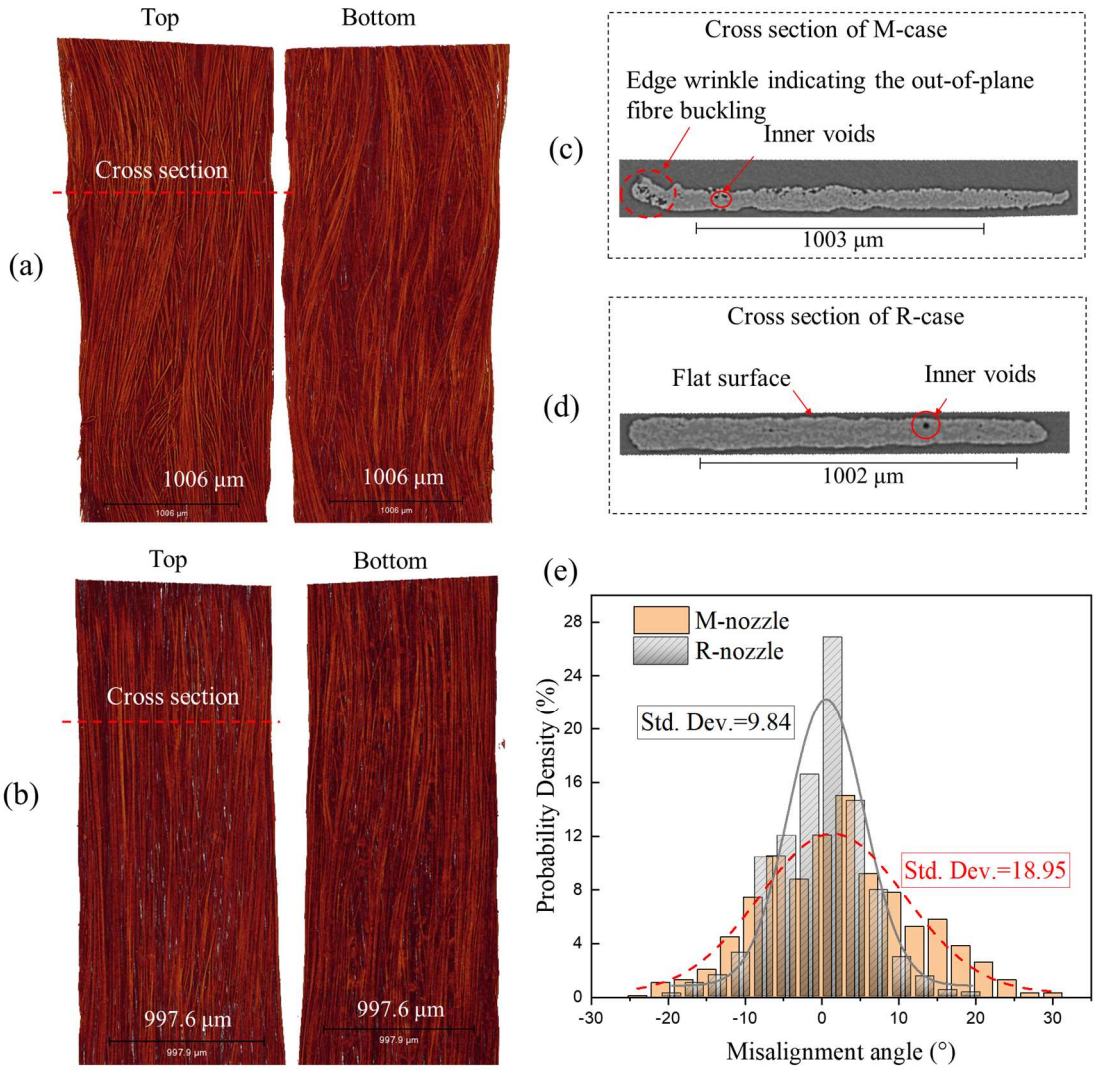

Fig. 6 X-ray µCT images of printed straight-line stripes: (a) & (c) M-nozzle, (b) & (d) R-nozzle, and (e) fibre misalignment angles of both cases.

µCT images of both printed stripes are reconstructed and processed in Avizo to trace individual fibres and quantify fibre misalignment. Specifically, a total number of five cross-sections are picked equally along the stripes to allow a statistical calculation of fibre orientations. As shown in Fig. 6e, the

misalignment angle of the M-nozzle case ranges from -25° to +25°, which is much larger than the range of R-nozzle case (±12°), with the standard deviation two times larger than the R-nozzle case. This proves that the AFD method has improved the fibre alignment to a certain content.

Representative cross-sections of both printed stripes are taken from the middle of each stripe and shown in Fig. 6c & d. For the M-nozzle case (see Fig. 6c), uneven edges are found on both top and bottom sides of the cross-section, showing rough surfaces are created by the irregular deformation of the filament at the nozzle-bed distance of 0.1 mm. More importantly, an edge wrinkle can be seen, showing the occurrence of out-of-plane fibre buckling and poor bonding with the bed. This seems to imply a non-uniform stress distribution within the placed tow, which could be caused by the uneven pressure from the ring-like nozzle tip. Much differently, the R-nozzle creates a flat surface on both top and bottom sides of the cross-section, as shown in Fig. 6d. This could benefit a good bonding with both the substrate and above layers and reduce air voids.

Some air voids can be seen inside the cross-section of stripes. The content of voids completely trapped inside the printed stripe is measured as 0.78% and 0.27% for M-nozzle and R-nozzle, respectively. Compared to the void content of the virgin filament, which is measured as 0.69% based on the CT image in Fig. 1a, it confirms the M-nozzle introduces more airs into the printed stripe. While the R-nozzle reduces the void content from 0.69% to 0.27%, showing the air voids are squeezed out during the deposition process.

From above results, it can be concluded that the R-nozzle substantially improves the deposition of continuous fibres during straight-line, in term of fibre alignment, tow morphology and air voids.

4.2 Curved line

In addition to the comparison of printing performance of both deposition methods for straight-line printing, this section compares the two deposition methods at specific curvature radii from 10.0 mm to 1.2 mm, in terms of fibre alignment, void content and fibre breakage that is prone to occur in curve-line than straight-line path.

4.2.1 Fibre alignment

At the *large* radius of 10.0 mm, R-nozzle produces a well-aligned tow than M-nozzle, as shown in Fig. 7. Fibre folding, fibre buckling, and fibre breakage apparently exist in the fibre bundle placed by M-nozzle (Fig. 7a). The M-nozzle tends to fold the fibres suddenly from the outer periphery to the inner, creating a fibre fold line extending from the middle of the bundle to the inner edge (as shown in Fig. 7a). Buckling fibres are produced at the folded position as the inner fibres are pushed to buckle when the filament twists inward from the outer periphery. Uneven tow width and teeth-like edges are also created by the tow twisting. By contrast, the R-nozzle produces a clear tow shearing line extending from the outside to the middle of the bundle (Fig. 7b), indicating the top fibres of the filament are shifted by the nozzle tip while the bottom fibres are bonded with the bed stably. This could imply the filament is subject to the shear load generated by the relative motion between the nozzle tip and the bed because of the rotational movement of the printer head. The tow shearing phenomenon seems to reduce the fibre wrinkling [29] and result in better fibre alignment. Even tow edges and tow width are consequently created by the aligned fibres. Moreover, the bottom view of the stripes is shown in Fig. A1 (Appendix A). This confirms that less fibre breakage and even tow wides are created by the AFD method than the traditional method.

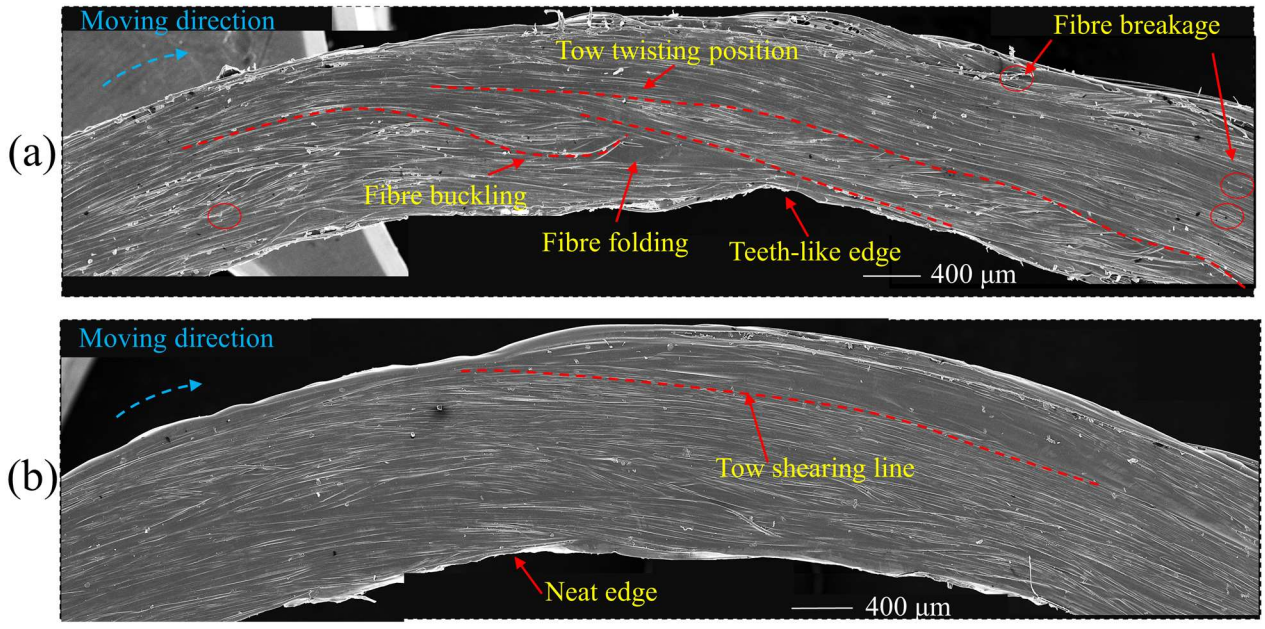

Fig. 7 Top view of 3D printed curved path with a radius of curvature R=10 mm: (a) M-nozzle and (b) R-nozzle.

For the *medium* curvature radii of 5.0 mm and 2.5 mm, multiple smaller events of fibre buckling are produced by M-nozzle at the inner periphery of the curved section (see Fig. 8a and Fig. A2), whilst relatively aligned fibres are found at the same position in the R-nozzle case (Fig. 8b). The occurrence

of inner buckling is probably because the M-nozzle squeezes the transition zone from the outside and creates buckling fibres. This phenomenon is not observed in the R-nozzle case probably because the nozzle always presses the filament along its moving direction. The excess fibre is found to be folded to the bottom from the inner periphery, as shown in Fig. A2 (Appendix A).

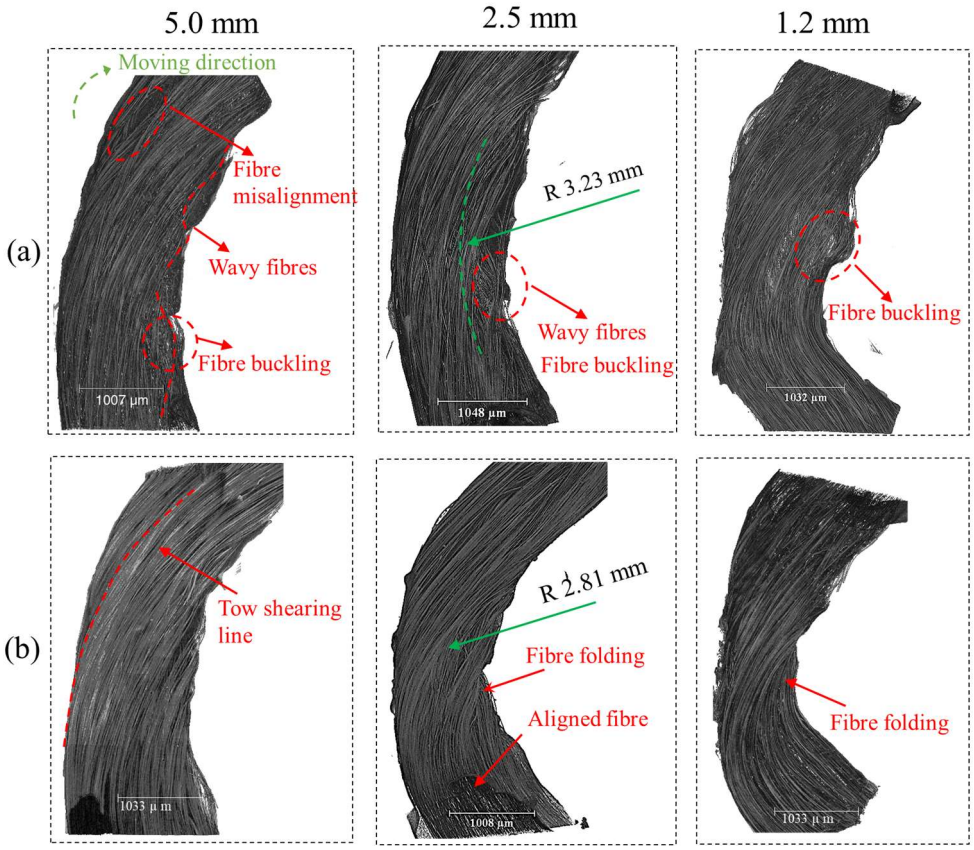

Fig. 8 X-ray µCT images (top views) of printed curved lines using (a) M-nozzle and (b) R-nozzle. (Only the central part of the curved stripes is cut and scanned.)

At a *small* radius of curvature of 1.2 mm, the M-nozzle creates a single and large defect of fibre buckling on the inner side of the curvature and unsmooth edge at the outer circumference, which indicates potential occurrence of tow debonding, as shown in Fig. 8a. By contrast, R-nozzle directly twists the filament and folds the fibres, indicating the filament is hard to be printed along an aligned direction at such a small radius of curvature. The results suggest that the printing of such small radius of 1.2 mm should be avoided for both deposition methods.

Besides the fibre alignment, the two nozzles produce different tow morphology. For example, the placement accuracy is found to be much improved by R-nozzle for the curved paths at those two increased radii of curvature, *e.g.*, R=2.81 mm by R-nozzle as compared to R=3.23 mm by M-nozzle for a real curvature radius of 2.5 mm, as shown in Fig. 8.

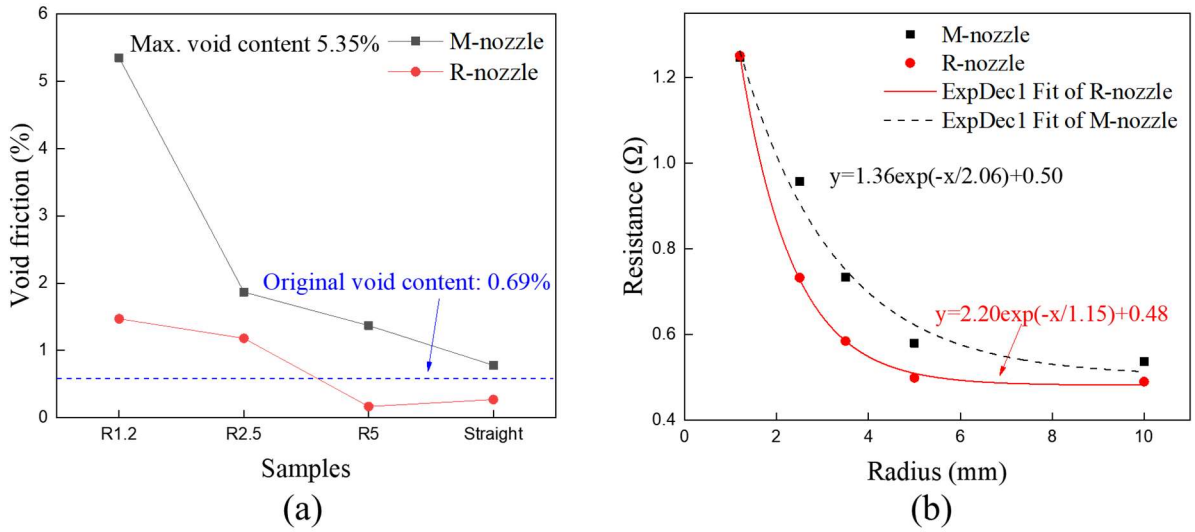

Fig. 9 (a) Air void content and (b) fibre electrical resistance at different radius of curvature.

In general, the R-nozzle helps improve the fibre alignment and hence the tow morphology at a large radius of curvature. The shifting of fibres becomes more dominating than fibre folding as the radius of curvature increases from 2.5 mm to 10.0 mm probably because of the friction of nozzle tip. Although the number of occurrences of fibre buckling is reduced by the M-nozzle as the radius of curvature is increased, noticeable fibre misalignment and fibre folding still exist.

4.2.2 Void content

As shown in Fig. 9a, the air voids inside the stripes decrease with increased radius of curvature. The void content in all M-nozzle cases is larger than the value of the virgin filament. The max void fraction (5.35%) is measured at the radius of 1.2 mm due to the paramount defects. The 5.0 mm radius case has fewer voids than other cases, but still more than the virgin filament. This means additional air voids are introduced into the fibre bundle by M-nozzle, probably because of the aggressive fibre movement it causes.

The void content in the R-nozzle cases is smaller than the M-nozzle cases at each radius. The void content is even less than the virgin filament when the radii of curvature are larger than 5.0 mm (0.17% compared to 0.69%). Its maximum void content is measured at the radius of 1.2 mm, which is almost 4 times lower than the same radius case of the M-nozzle (1.47% to 5.35%). By the values calculated for both straight-line and curved-line cases, it is reasonable to conclude that the AFD with R-nozzle reduces the air void contents during the fibre deposition.

4.2.3 Fibre breakage

Electrical resistances are measured to evaluate the fibre breakages caused by the printing processes based on the method reported in Ref. [15]. As shown in Fig. 9b, the fibre electrical resistances decrease to certain values and the fitted curve tends to be flattened as the radii are larger than 5.0 mm, but the value increases dramatically when the printing radius decreases below 5.0 mm. This indicates more fibre breakages are resulted during the placement along small radius paths. Apparently, the M-nozzle cases have larger electrical resistance values compared to their competitors, except for the 1.2 mm case, where the two deposition methods have similar values. The results imply that more excessive fibre breakages are produced by the M-nozzle than the R-nozzle. However, both nozzles induce large defects hence large number of fibre breakages when the printing radii are small enough, *i.e*. 1.2 mm. By inspecting the SEM images of 10.0 mm cases, more fibre breakages are counted in the M-nozzle cases and are marked by red circles (as shown in Fig. 7 and Fig. A1), which also echoes the electrical resistance results. The fibre breakages seem to occur in tandem with violent fibre waviness. For example, more fibre breakages are found at the edge or on the bottom of the curved stripes especially, probably because of the occurrence of excessive fibre waviness. The AFD with R-nozzle produces less fibre waviness hence fewer fibre breakages along both straight-line and curved-line paths.

5. Deposition mechanisms

In this section, the transition zone of the deformed filament is experimentally observed to understand the fibre movement, and the printing process is numerically simulated with a FEM model that provides the strain and stress distributions in the transition zone as well as the printed stripes. The differences of deposition mechanisms between both deposition methods are then identified, and particularly the formation of in-plane fibre waviness and fibre folding is explained.

5.1 Printing along a straight-line path

The filament bends at the transition zone during straight-line printing, *i.e.,* angular position of 0°. SEM images are captured from the top and the bottom of this area, as shown in Fig. 10. The FE modelling results of this zone are shown in Fig. 11 and Fig. 12, to compare with the experimental observation results.

5.1.1 Experimental observations

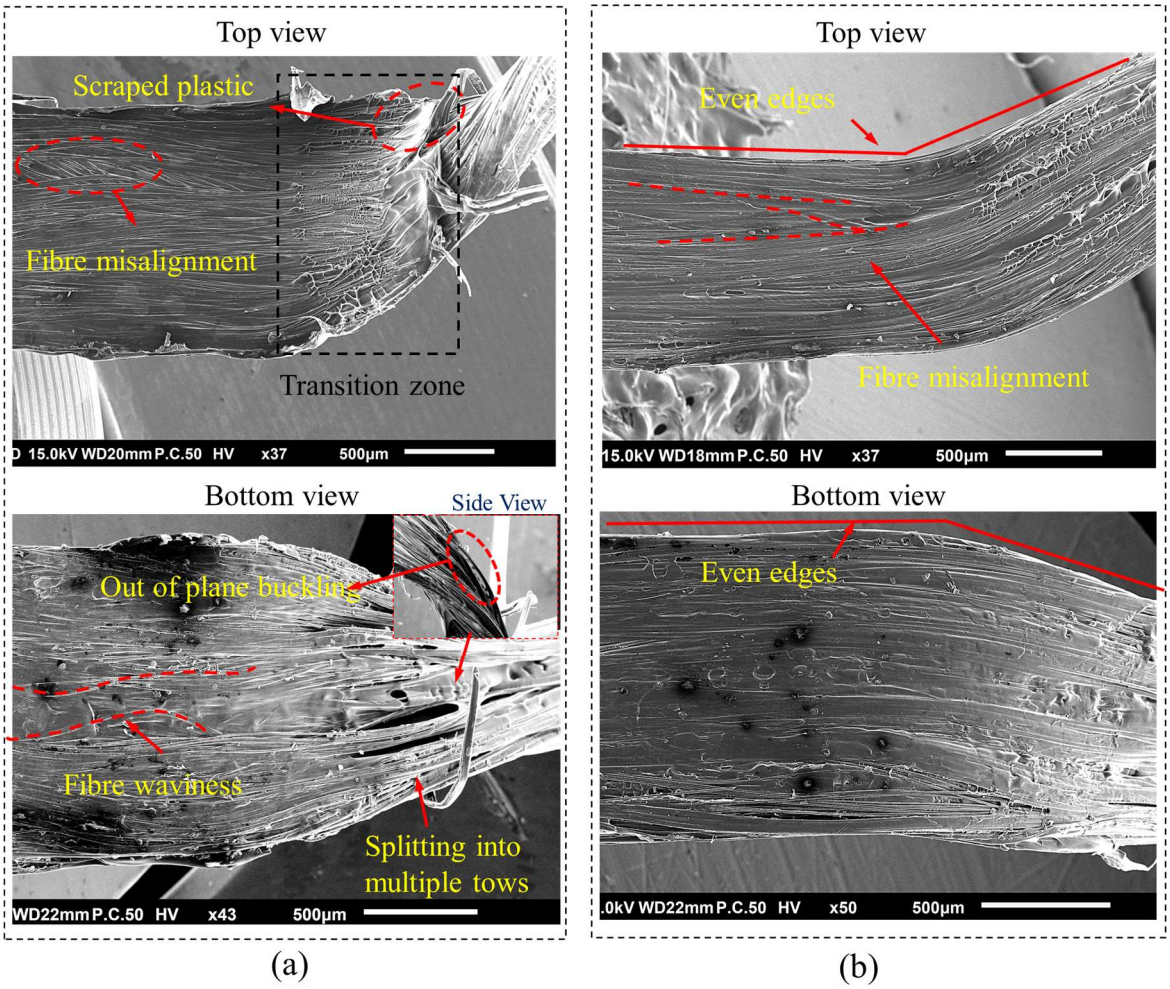

Fig. 10 SEM images of the composite filament deposited at 0° angle position: (a) M-nozzle and (b) R-nozzle. (Some small dark spots appear in the images, probably due to dusts or impurities)

As shown in Fig. 10a, the filament elbow created by M-nozzle deforms dramatically in the transition zone. The fibre bundle spreads from the middle to both sides with slight fibre waviness. In the middle of the stripe, some unaligned fibres can be found underneath those visible fibres on the top surface, indicating the occurrence of fibre misalignment. Meanwhile, melted plastic is scraped forward by the nozzle tip and flows from the stripe edges to the middle, indicating large friction is caused by the conical shape of the M-nozzle outlet. The scratched plastic results in uneven matrix distribution in the final part and would weaken the interlayer bonding. When observing from the bottom, the stripe is found to be split into multiple bundles in the transition zone, leading to large gaps and air voids. The fibres wave severely on the convex side of the elbow with occasional out-of-plane fibre buckling, resulting in uneven edges of the stripe. More paramount fibre waviness and fibre misalignment can be seen on the bottom surface, which is exactly caused by the fibre buckling in the transition zone.

For the case of AFD with R-nozzle, the fibres are deposited evenly from the inclined passage of the nozzle to the bed and no noticeable fibre waviness occurs after deposition (see Fig. 10b), resulting in straight edges and consistent stripe width. The melted plastic is more evenly distributed and shows a smoother finish surface than the result of the M-nozzle. Slight fibre misalignment is also found in the middle of the stripe, similar to the phenomenon occurring in the case of M-nozzle, perhaps because of large compressive deformation hence greater fibre movement in the middle of the filament. The bottom fibres are also better aligned than its competitor, with even stripe edges and a smooth finish surface. No visible cracks appear in the transition zone, which explains why R-nozzle produces fewer air voids than M-nozzle as discussed in Section 4.1.

In general, the filament deforms much more gently in the transition zone in R-nozzle than in M-nozzle, thanks to the smaller feeding angle (*i.e.*, 45° in R-nozzle as compared to 90° in M-nozzle) and large bending radius which reduces the filament's deformation and fibre misalignment. The rectangular nozzle edge of R-nozzle also provides even pressure on the filament. The stripe surfaces are found to be smoother, and the plastic matrix is more evenly distributed over the fibres.

5.1.2 Finite element modelling

The straight-line printing mechanisms are further discussed and interpreted using the developed FE model, with a focus on the deformation in the filament in terms of plastic strain distributions. The distributions of PE22 shown in Fig. 11 indicates how the heated filament is pressed by the nozzle and expanded in the width direction due to the Poisson effect. The transverse tensile/compressive plastic strain in the width direction indicates the spread of the fibres and is used to reveal the degree of fibre misalignment. The obvious difference in the distributions is found to be on the top surface of the printed stripe (circled in black in Fig. 11a), in which the M-nozzle exhibits an uneven distribution and a much smaller value of PE22 as compared to the R-nozzle. This explains the difference in the fibre alignment and the flow of plastic as seen in the experimental observations in Fig. 10. Besides, both two nozzles exhibit more uneven distributions of PE22 on the bottom surface than on the top surface. As for the R-nozzle, although most of the elements are under higher tension, slight irregularity is caused by the fluctuating cohesive interaction with the bed as the filament keeps being

stretched by the moving nozzle. However, the irregularity of PE22 distribution is aggravated on the bottom surface of the printed stripe by M-nozzle, due to the non-uniform contact pressure exerted from the ring-like nozzle tip of M-nozzle (as shown in Fig. 11a). The uneven distribution of PE22 also indicates more fibre misalignment on the bottom surface, which is in good agreement with the experimental observations in Fig. 10a.

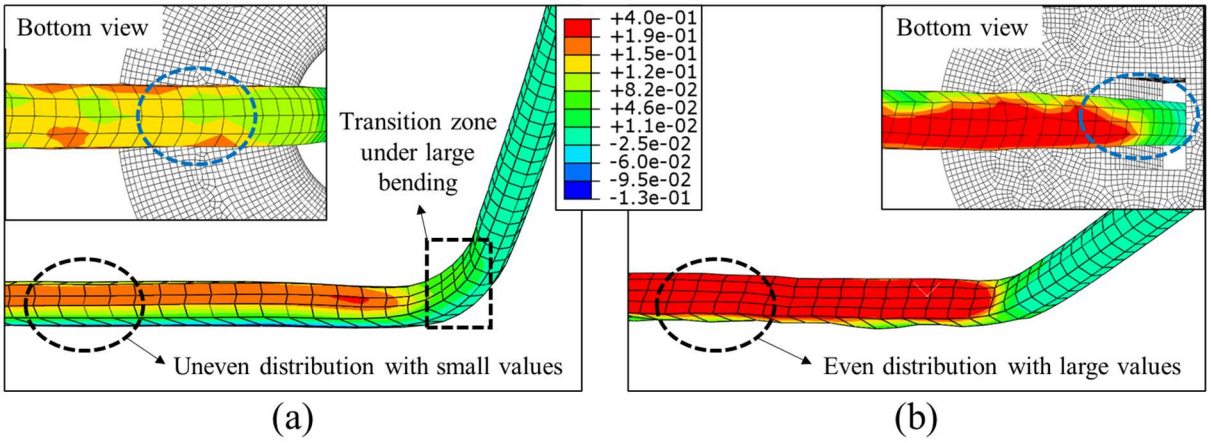

Fig. 11 Transverse normal plastic strain PE22 when printing a straight path: (a) M-nozzle and (b) R-nozzle

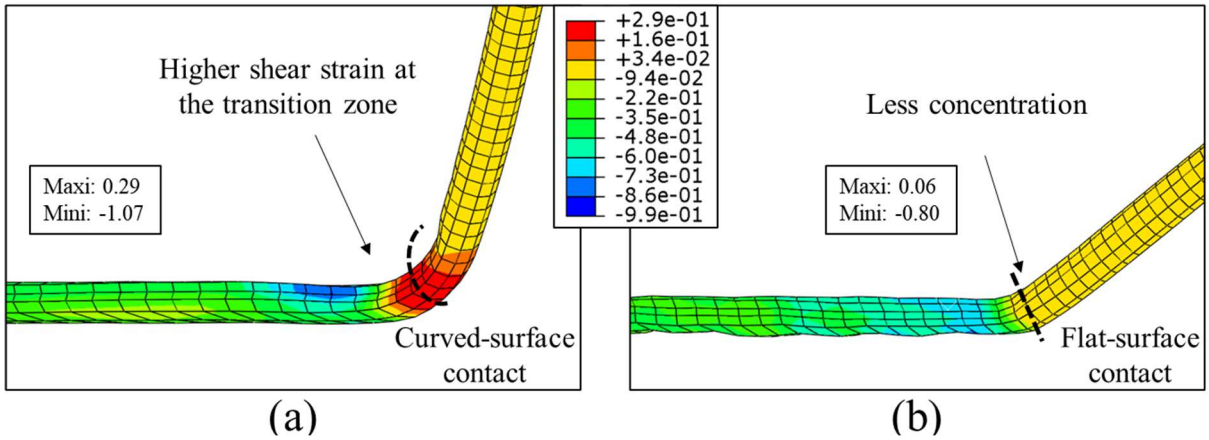

Fig. 12 Transverse shear plastic strain PE13 when printing a straight path: (a) M-nozzle and (b) R-nozzle.

Another different characteristic between these two nozzles is the transition zone in the filament before being printed on the bed. A sharp transition zone under large bending is observed in the case of M-nozzle (framed in Fig. 12a), which exactly indicates the splitting and out-of-plane buckling of the fibre tow presented in the experimental result (as shown in Fig. 10a). This is also evidenced by a higher transverse shear strain PE13 in this region, as shown in Fig. 12a. On the contrary, such a transition zone is not noticeable when it comes to the R-nozzle, confirming the printing defects are reduced when printing a straight-line path using R-nozzle with a smaller, inclined feeding angle.

From the above results, it is understood that the in-plane fibre misalignment of the M-nozzle is mainly caused by the severe bending deformation due to the small bending radius. Similar phenomenon also

occurs in other manufacturing processes of thermoplastic composites, for instance, the stamp forming process [30]. More specifically, the fibre waviness in our experiment occurs on the convex side of the elbow, similar to those processes using a male mould [31], probably because the filament is pulled to the nozzle and this tension makes the fibres on the convex side easier to be split, resulting in out-of-plane waviness. As the waved fibres are pressed by the forward-moving nozzle, they will then form the in-plane fibre waviness and/or misalignment as observed in the experiment.

5.2 Printing along curved-line paths

The printed stripes are captured at angular positions of 45°, 90°, 135° and 180° on a curved-line path with a curvature radius of 2.5 mm for both deposition methods. The deposition process of the entire curved-line path is also simulated by the FEM model with results extracted at the same pause positions to compare with the experimental observations.

5.2.1 Experimental observations

Fig. 13 shows the instantaneous fibre alignment captured from the paused positions in the curved-line deposition for both deposition methods at a curvature radius of 2.5 mm. All images are obtained from the bottom view of the stripe and the nozzle turns in the clockwise direction. The transition zone is included in the images to better illustrate how the filament evolves into a curved stripe during the printing.

The SEM image at the angular position of 45° presents the situation when the bundle starts turning. A slight torsional deformation of filament is found just above the stretched elbow for the M-nozzle, resulting in significant fibre waviness. This torsion of filament is probably derived from the friction of the M-nozzle due to its non-rotational movement. During the deposition of a curved line, the filament needs to rotate along the curved path to keep the fibre aligning with the path, otherwise, a torque or twisting moment would be imposed on the pre-printing filament by the printed-on-bed part. If the filament is free to rotate during printing, this torque would be released. However, the filament's rotation is restricted by the PTFE guide tube and its long feeding tail in the experiment, even though the extrusion end is deliberately set free. In the worst case, the inversion of the inner and outer circumferences of the fibre bundle would occur at least once when half a circle is printed [13], and

this is hard to avoid when using this printing method with the M-nozzle. In comparison, better fibre alignment is produced by the R-nozzle at the same angular position (Fig. 13b). No torsional deformation of filament occurs, presumably just because the filament rotates together with the hot-end and the R-nozzle always presses the filament along its deposition direction. The transition elbow looks like a neat crease line that slightly leans forward along the printing path, in contrast to the irregular shape in the M-nozzle case.

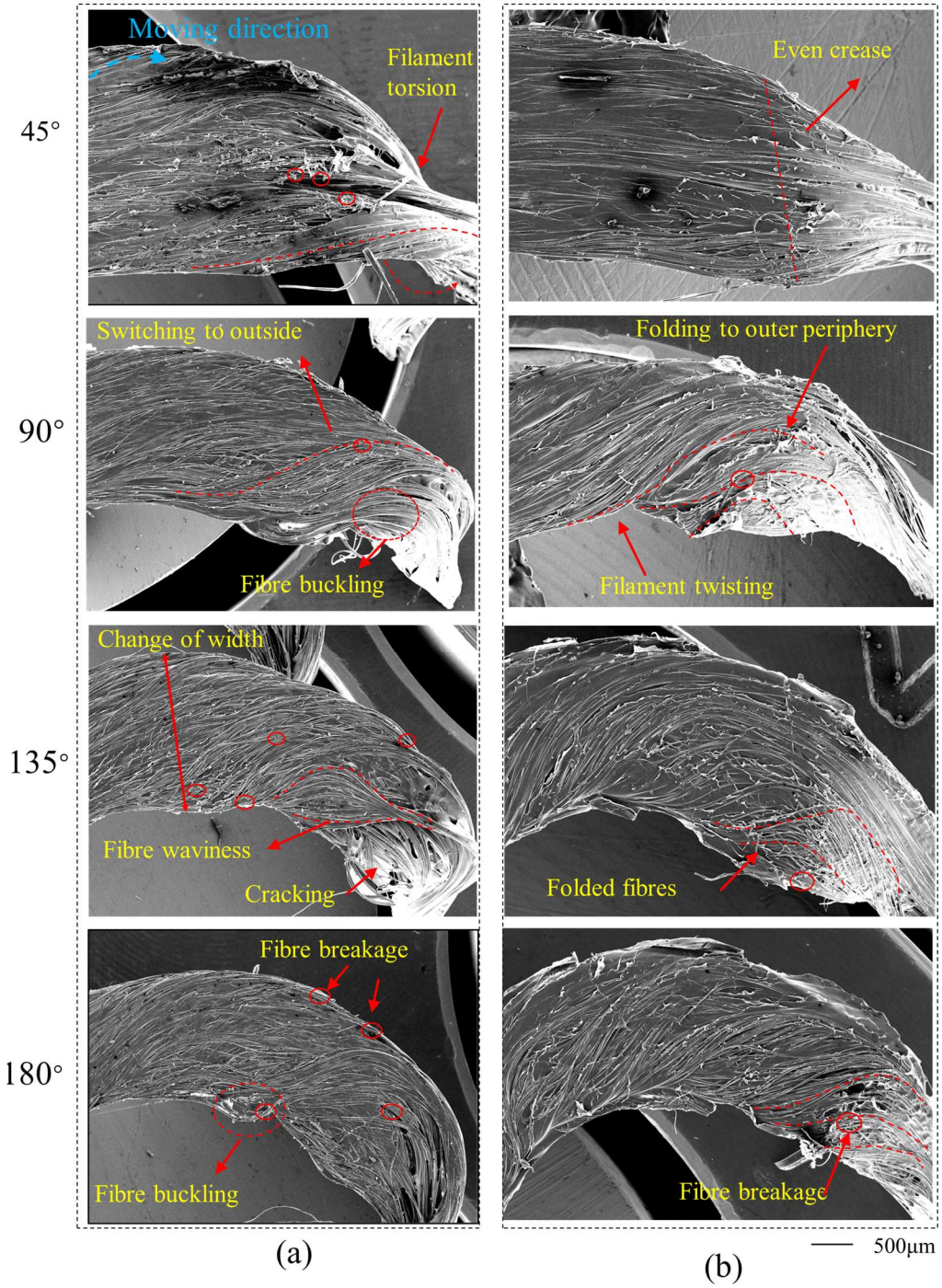

Fig. 13 Bottom view of the printed stripes at angular positions of 45°, 90°, 135° and 180° of (a) M-nozzle and (b) R-nozzle. (The fibre breakage is marked with red solid circles.)

At the angular position of 90°, M-nozzle creates evident fibre buckling at the inner periphery, while the R-nozzle folds the fibres to the middle of the bundle. The M-nozzle pushes the deformed elbow out of the circumference by its outlet surface, leading to the occurrence of fibre buckling and hence the sudden increase of tow width (90°, Fig. 13a). It suggests that the inner fibres are under compression, resulting in excessive length than the outer periphery. The excessive length fibres tend to kink and wrinkle. Compared to the buckling fibres caused by M-nozzle, the fibres with excessive length are swept to the outside of the circumference by R-nozzle in the transition zone. These fibres are probably swept by the bed towards the outside of the circumference before fully consolidating on the bed, creating an even tow width and neat edges hence then. The folded fibres could mitigate the fibre wrinkling that normally occurs in the curved-line placement by AFP/ATP [23, 32], but may cause fibre breakage because of the extensive fibre waviness.

Much serious filament cracking can be seen when the angular position of the M-nozzle is beyond 135° (Fig. 13 a), introducing air voids into the printed stripe and causing dramatic fibre waviness and breakage. More specifically, the top fibres are peeled off from the bed-bonding fibres and folded from the outer periphery to the inner (see the cracking at 135°). Both the above-mentioned torsion and shearing force generated by the M-nozzle are presumably the main causes of the cracking. The torsional deformation promotes the fibre waviness while the friction between the filament and the nozzle tip tends to shear the printing filament and bring the top fibres to the inner periphery, indicating the moving direction of the M-nozzle is inclined to the inside radius during a curved-line deposition. No cracking is found in the case of R-nozzle which explains fewer air void and less fibre breakage of R-nozzle case in section 4.2.2

Fibre breakage is inspected and marked with red solid circles in all images. The results show that the fibre breakage normally occurs at the edges of the printed stripe and/or at positions where fibres wave dramatically, which is likely caused by excessive fibre buckling. Moreover, M-nozzle generally causes more fibre breakage than R-nozzle, which is reasonably expected because of the aggressive fibre movement produced by M-nozzle.

5.2.2 Finite element modelling

(a) Torsional deformation in the pre-printing filament

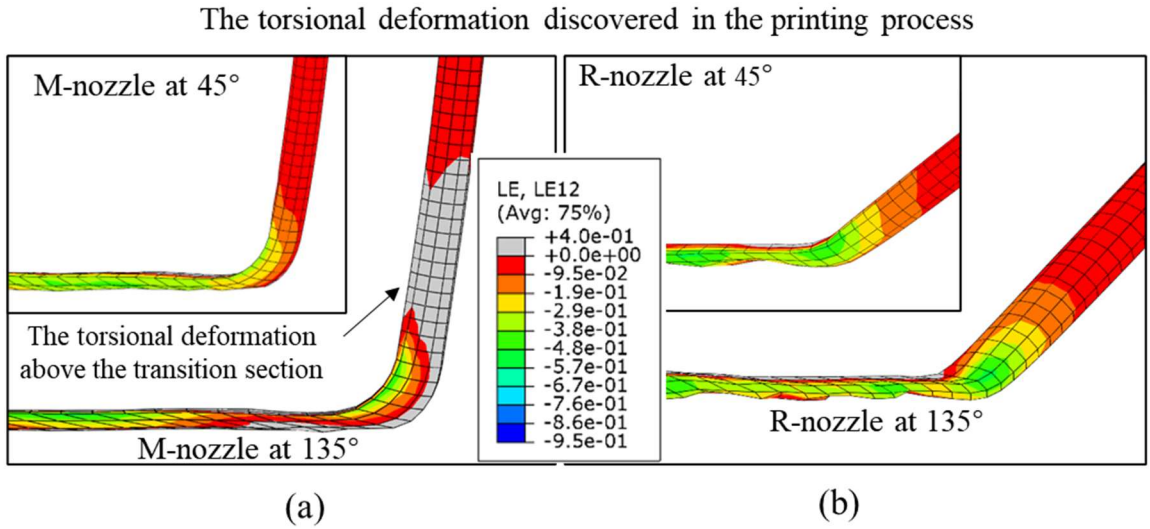

Fig. 14 Distribution of logarithmic strain component LE12 at angles 45° and 135° on the printed curved-line path with a radius of curvature of 2.5 mm.

The torsional deformation in the pre-printing filament above the transition zone can also be clearly seen in the modelling. In the following analysis, shear strains with positive and negative values are plotted out in grey and colours, respectively, for better clarification of the distributions. Since the torsional deformation is relatively small inside the PTFE tube and almost no plastic deformation occurs there as the filament is thermally insulated by the PTFE tube, the distribution of logarithmic strain (LE) is used for this analysis. As shown in Fig. 14, extremely small values of LE12 (in red colour) are found above the transition zone in the simulation frames at 45° and 135° angles for R-nozzle. As for the M-nozzle, the distribution at the 45° angular position is similar to that of the R-nozzle since less filament twisting happens at this point, but positive values are observed at the 135° angle for M-nozzle, indicating the torsional deformation in the filament before being printed. It explains that the torsional deformation only occurs when the twisting of printed filament happens, and it is caused by the relative motion between the twisted printed stripe and the pre-printing filament that is constrained at the far end.

(b) Fibre twisting in the printed stripe

Since the composite filament is considered as a homogeneous, transversely isotropic material in the FE modelling, the twisting of the filament is concerned rather than the twisting of individual fibres. In addition, the torsional deformation of filament and tow shearing caused by the friction with the nozzle tip will be numerically analysed. The transverse normal strain PE22 in the width direction is

believed to more appropriately indicate the in-plane fibre distribution in the printed stripe, while the transverse shear strain PE23 is believed to indicate the overall filament twisting, respectively.

The distribution of transverse normal strain PE22 with the curvature radius of 10 mm for these two nozzles is presented in Fig. 15, in which the second material orientation of the elements is indicated by blue arrows. As for the M-nozzle, no noticeable change of fibre alignment is seen at the beginning of the curved section, followed by a gradual filament twisting at an angular position in-between 45°-60° that continues for the rest of the curved printing path. However, no filament twisting can be found for the R-nozzle and the filament edges keep aligned along the entire curved path, which can be illustrated by the consistency of the second material orientation. M-nozzle exhibits a more irregular distribution of PE22, with the maximum value located at an angular position in-between 80°-90°, which is likely caused by the excessive friction from the nozzle tip because of the relative motion between the filament and the M-nozzle (the details can be found in Fig. A3). Although some mutation points exist in the case of R-nozzle due to the adopted sub-step approach (*i.e.*, the numerical step for printing a curved path is divided into 12 sub-steps in the modelling), apparently much more regular distribution of PE22 is observed. Clearly, this will result in a more consistent printed width during the printing of a curved path, which is also revealed by the experimental observation in Fig. 7b.

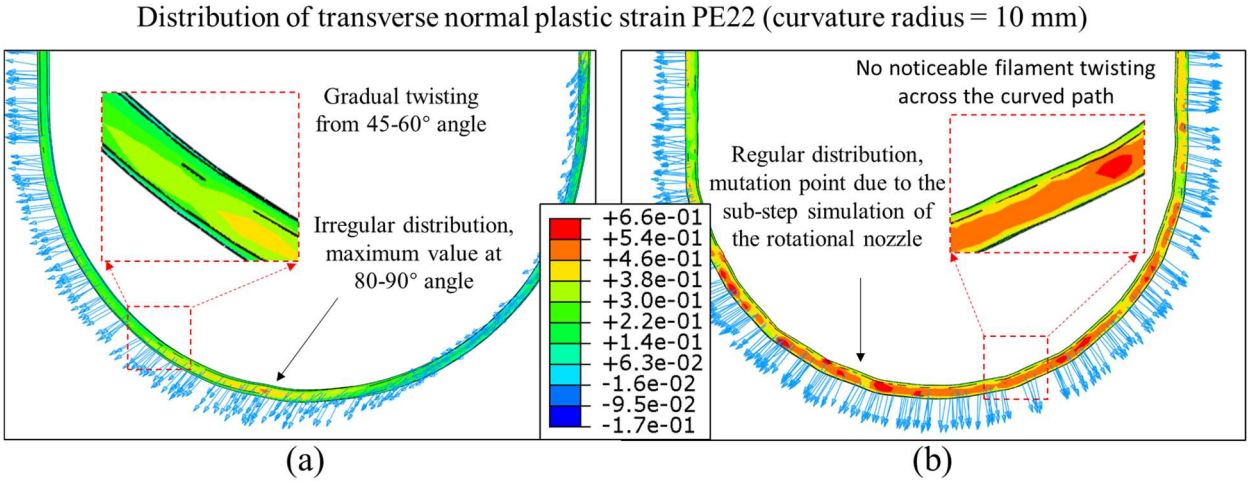

Fig. 15 Distribution of transverse normal plastic strain PE22 when printing a curved path with a radius of curvature of 10 mm: (a) M-nozzle and (b) R-nozzle.

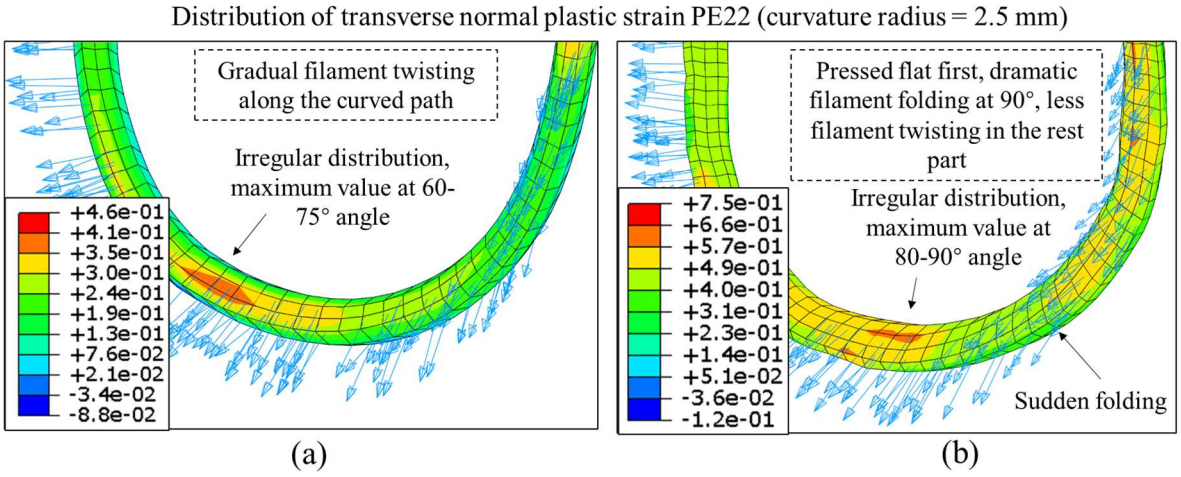

Fig. 16 Distribution of transverse normal plastic strain PE22 when printing a curved path with a radius of curvature of 2.5 mm: (a) M-nozzle and (b) R-nozzle.

The printing process with a small curvature radius of 2.5 mm is also simulated. As shown in Fig. 16a, a similar pattern of PE22 is observed for M-nozzle, but the gradual filament twisting exists across the entire curved path and the location of the maximum PE22 occurs earlier than in the 10 mm case, indicating a more severe fibre twisting inside the filament. However, the deposition result changes more significantly for the R-nozzle while printing a curved path with such a small curvature radius. The R-nozzle tends to press the heated filament flat by its side surface of outlet, and the occurrence of filament twisting cannot be suppressed under such a small curvature radius. Therefore, a dramatic filament twisting (more like the filament twisting in the 90° result of Fig. 8b of experimental observation) occurs approximately in the middle of the curve where the maximum PE22 is found, followed by the sudden change of the material orientation. After that, little filament twisting occurs in the rest part of the curved path.

The transverse shear strain PE23 is calculated based on the absolute value at different angular positions in the curved section. It should be clarified that this is not a standard quantitative analysis but a comparison of the evolution of misalignment and twisting, because the material properties in the modelling cannot be accurately defined yet. As shown in Fig. 17a, PE23 of M-nozzle increase gradually and then come to their peaks at an angular position in-between 80°-100°. As for the R-nozzle, the curves show small fluctuations, indicating less twisting occurs in the whole process with the 10 mm curvature radius, thanks to the assistance of the rotational printer head in the AFD system. As for the curvature radius of 2.5 mm, a similar pattern is observed in the printing using M-nozzle

(with similar peak location and value) as shown in Fig. 17b. However, a sharp rise can be observed for the R-nozzle at the 60° angular position for PE23 and then it reaches a higher peak value than that in the 10 mm case. This is followed by a sharp drop to reach the next lowest value at about 100° angular position. This echoes the sudden change of the second material orientation (as observed in Fig. 16b above) and the dramatic fibre twisting (more like a fibre folding in Fig. 8b of experimental observation) at an angular position in-between 80°-90°.

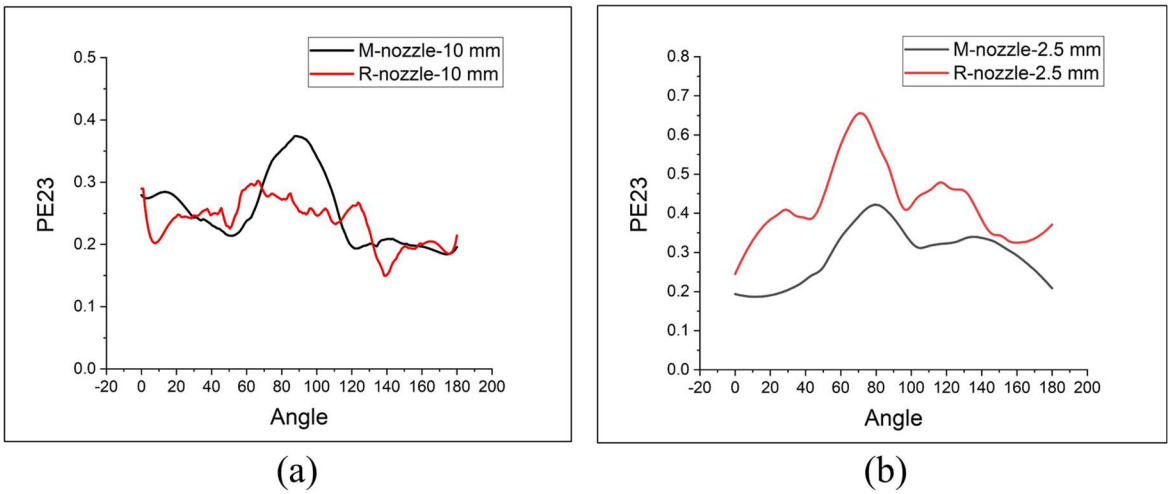

(a) (b)

Fig. 17 Evolution of transverse shear plastic strain PE23 when printing a curved path with a radius of curvature of (a) 10 mm and (b) 2.5 mm.

(c) Dynamic interaction between nozzle and filament

The evolution of the friction force (*i.e.*, the reaction force of the nozzle in the radial direction of the curved path) for the whole printing process is extracted and presented in. It can be seen that the M-nozzle exhibits a generally higher friction force compared with the R-nozzle, in the printing with both curvature radii of 10 mm and 2.5 mm. This indicates the inclined feeding angle in R-nozzle can efficiently reduce the friction between the filament and the nozzle tip when printing with curvature, and thus mitigate the manufacturing defects such as filament twisting and fibre waviness. In addition, a stronger fluctuation can be found in the curves of the R-nozzle. It is caused by the R-nozzle's rectangular outlet with a smaller width and the associated collision between the filament and the inner edges of the nozzle in the FE modelling. On the contrary, kinetic friction happens in the printing process with the M-nozzle, which is accompanied by the slipping of contact and the shifting movement of the M-nozzle, thus resulting in smaller fluctuations in the curves. A more detailed

visualisation of the nozzle-filament interaction before and after an angular position of 90° can be found in Appendix B.

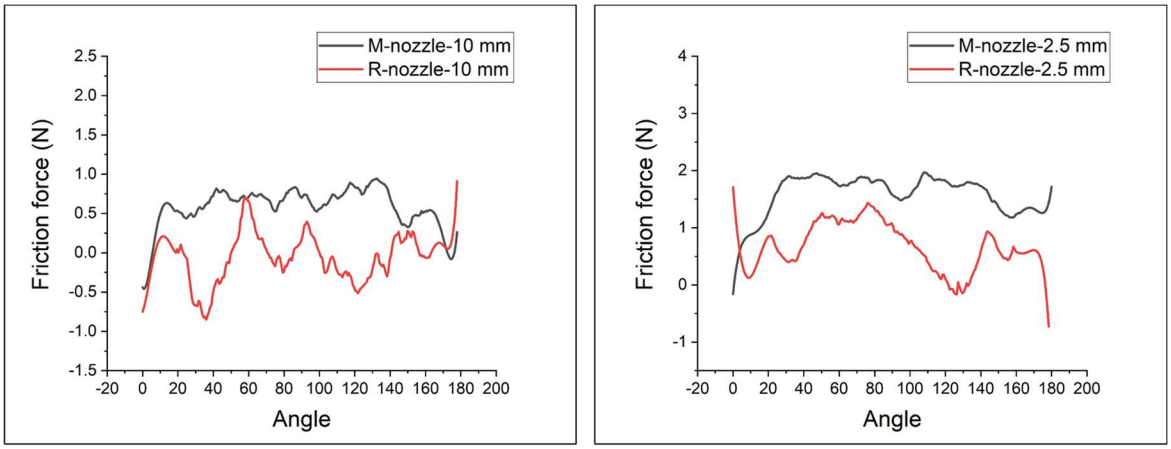

(a) (b)

Fig. 18 Evolution of friction force when printing a curved path with a radius of curvature of (a) 10 mm and (b) 2.5 mm.

In summary, no clear filament cracking and fibre twisting are found in the R-nozzle case, thanks to the rotation of the R-nozzle as well as the consistent nozzle-filament. Although the fibre folding occurs when printing at a 2.5 mm radius path, R-nozzle produces fine filament placement with even strain distribution at a large radius path (10.0 mm) compared to M-nozzle. Torsional deformation in the pre-printing filament is found for M-nozzle, which could be one of the main reasons for excessive fibre movement.

6. Conclusions

This paper presents a novel aligned fibre deposition (AFD) method for 3D printing of continuous carbon fibre reinforced thermoplastic composites using a novel customised printer nozzle. Compared to a traditional deposition method with a commercial vertical feeding nozzle, the developed AFD system shows satisfactory improvement of fibre alignment in printing both straight-line and curved-line paths. The improved fibre architecture in this study will be reflected on the mechanical properties of printed composite and deserves further investigation. Based on the experimental characterisations and finite element modelling, main conclusions are drawn as below:

(1) The R-nozzle used in AFD method with a large bending radius mitigates severe deformation of fibre bundle and avoids the crack of the filament, resulting better fibre alignment, few air voids and less fibre breakage.

(2) The torsional deformation in the pre-printed filament is eliminated by the AFD method due to the rotational movement. The rectangular outlet presses the filament along the moving direction, providing even strain distributions and less friction.

(3) Fibre twisting caused by both the torsion of filament and the shearing from the nozzle tip in traditional deposition method is replaced by tow shearing in AFD method at large radii of curvature printing. However, deposition along a small radius (R=1.2 mm) should be avoided for both methods.

Acknowledgement

The authors would like to acknowledge EPSRC CIMComp Hub (EP/P006701/1-RIS3718946) for financial support of this research project.

References

[1] Parandoush P, Lin D. A review on additive manufacturing of polymer-fiber composites. Composite Structures. 2017;182:36-53.
[2] MarkForged. accessed: April 2021.
[3] Van De Werken N, Tekinalp H, Khanbolouki P, Ozcan S, Williams A, Tehrani M. Additively manufactured carbon fiber-reinforced composites: State of the art and perspective. Additive Manufacturing. 2020;31:100962.
[4] Matsuzaki R, Ueda M, Namiki M, Jeong TK, Asahara H, Horiguchi K, et al. Three-dimensional printing of continuous-fiber composites by in-nozzle impregnation. Sci Rep. 2016;6:23058.
[5] Yang C, Tian X, Liu T, Cao Y, Li D. 3D printing for continuous fiber reinforced thermoplastic composites: mechanism and performance. Rapid Prototyping Journal. 2017;23(1):209-15.
[6] Zhang K, Zhang W, Ding X. Multi-axis additive manufacturing process for continuous fibre reinforced composite parts. Procedia CIRP. 2019;85:114-20.
[7] Kabir SMF, Mathur K, Seyam A-FM. A critical review on 3D printed continuous fiber-reinforced composites: History, mechanism, materials and properties. Composite Structures. 2020;232:111476.
[8] Lukaszewicz D, Ward C, Potter KD. The engineering aspects of automated prepreg layup: History, present and future. Compos Pt B-Eng. 2012;43(3):997-1009.
[9] Chen X, Fang G, Liao W-H, Wang CCL. Field-Based Toolpath Generation for 3D Printing Continuous Fibre Reinforced Thermoplastic Composites. Additive Manufacturing. 2021:102470.
[10] Zhang H, Chen J, Yang D. Fibre misalignment and breakage in 3D printing of continuous carbon fibre reinforced thermoplastic composites. Additive Manufacturing. 2021;38:101775.
[11] Hu Y, Ladani RB, Brandt M, Li Y, Mouritz AP. Carbon fibre damage during 3d printing of polymer matrix laminates using the fdm process. Materials & Design. 2021:109679.
[12] Galos J, Hu Y, Ravindran AR, Ladani RB, Mouritz AP. Electrical properties of 3D printed continuous carbon fibre composites made using the FDM process. Composites Part A: Applied Science and Manufacturing. 2021;151:106661.
[13] Matsuzaki R, Nakamura T, Sugiyama K, Ueda M, Todoroki A, Hirano Y, et al. Effects of Set Curvature and Fiber Bundle Size on the Printed Radius of Curvature by a Continuous Carbon Fiber Composite 3D Printer. Additive Manufacturing. 2018;24:93-102.

[14] Latil P, Orgéas L, Geindreau C, Dumont PJJ, Rolland du Roscoat S. Towards the 3D in situ characterisation of deformation micro-mechanisms within a compressed bundle of fibres. Composites Science and Technology. 2011;71(4):480-8.
[15] Shiratori H, Todoroki A, Ueda M, Matsuzaki R, Hirano Y. Mechanism of folding a fiber bundle in the curved section of 3D printed carbon fiber reinforced plastics. Adv Compos Mater. 2020;29(3):247-57.
[16] Clancy G, Peeters D, Oliveri V, Jones D, O'Higgins RM, Weaver PM. A study of the influence of processing parameters on steering of carbon Fibre/PEEK tapes using laser-assisted tape placement. Composites Part B: Engineering. 2019;163:243-51.
[17] Li N, Link G, Jelonnek J. 3D microwave printing temperature control of continuous carbon fiber reinforced composites. Composites Science and Technology. 2020;187:107939.
[18] Zhuo P, Li S, Ashcroft IA, Jones AI. Material extrusion additive manufacturing of continuous fibre reinforced polymer matrix composites: A review and outlook. Composites Part B: Engineering. 2021:109143.
[19] Parker M, Inthavong A, Law E, Waddell S, Ezeokeke N, Matsuzaki R, et al. 3D Printing of Continuous Carbon Fiber Reinforced Polyphenylene Sulfide: Exploring Printability and Importance of Fiber Volume Fraction. Additive Manufacturing. 2022:102763.
[20] Toll S. Packing mechanics of fiber reinforcements. Polymer Engineering & Science. 1998;38(8):1337-50.
[21] Durville D. Numerical simulation of entangled materials mechanical properties. Journal of Materials Science. 2005;40(22):5941-8.
[22] Stewart AL, Poursartip A. Characterization of fibre alignment in as-received aerospace grade unidirectional prepreg. Composites Part A: Applied Science and Manufacturing. 2018;112:239-49.
[23] Bakhshi N, Hojjati M. An experimental and simulative study on the defects appeared during tow steering in automated fiber placement. Composites Part A: Applied Science and Manufacturing. 2018;113:122-31.
[24] Chabaud G, Castro M, Denoual C, Le Duigou A. Hygromechanical properties of 3D printed continuous carbon and glass fibre reinforced polyamide composite for outdoor structural applications. Additive Manufacturing. 2019;26:94-105.
[25] Blok LG, Longana ML, Yu H, Woods BKS. An investigation into 3D printing of fibre reinforced thermoplastic composites. Additive Manufacturing. 2018;22:176-86.
[26] He Q, Wang H, Fu K, Ye L. 3D printed continuous CF/PA6 composites: Effect of microscopic voids on mechanical performance. Composites Science and Technology. 2020;191:108077.
[27] Continuous Composites.
[28] Wang D, Naouar N, Vidal-Salle E, Boisse P. Longitudinal compression and Poisson ratio of fiber yarns in meso-scale finite element modeling of composite reinforcements. Composites Part B: Engineering. 2018;141:9-19.
[29] Kim BC, Potter K, Weaver PM. Continuous tow shearing for manufacturing variable angle tow composites. Compos Part a-Appl S. 2012;43(8):1347-56.
[30] Sitohang RDR, Grouve WJB, Warnet LL, Akkerman R. Effect of in-plane fiber waviness defects on the compressive properties of quasi-isotropic thermoplastic composites. Composite Structures. 2021;272:114166.
[31] ÇINAR K. Influences of out-of-plane fiber waviness on the curved beam strength of glass fiber composite laminates Düzlem dışı fiber dalgalanmasının cam elyaf takviyeli tabakalı kompozitlerin kavisli kiriş dayanımı üzerindeki etkileri.
[32] Rajan S, Sutton MA, Wehbe R, Tatting B, Gürdal Z, Kidane A, et al. Experimental investigation of prepreg slit tape wrinkling during automated fiber placement process using StereoDIC. Composites Part B: Engineering. 2019;160:546-57.